JACS
JOURNAL OF THE AMERICAN CHEMICAL SOCIETY

ARTICLE

pubs.acs.org/JACS

Synthesis, Structural Transformation, Thermal Stability, Valence State, and Magnetic and Electronic Properties of $PbNiO_3$ with Perovskite- and $LiNbO_3$-Type Structures

Yoshiyuki Inaguma,*[,†] Kie Tanaka,[†] Takeshi Tsuchiya,[†] Daisuke Mori,[†] Tetsuhiro Katsumata,[§] Tomonori Ohba,[∥] Ko-ichi Hiraki,[‡] Toshihiro Takahashi,[‡] and Hiroyuki Saitoh[⊥]

[†]Department of Chemistry, and [‡]Department of Physics, Faculty of Science, Gakushuin University, 1-5-1 Mejiro, Toshima-ku, Tokyo 171-8588, Japan

[§]Department of Chemistry, School of Science, Tokai University, 4-1-1 Kitakaname, Hiratsuka, Kanagawa 259-1292, Japan

[∥]Department of Chemistry, Graduate School of Science, Chiba University, 1-33 Yayoi, Inage, Chiba 263-8522, Japan

[⊥]Japan Atomic Energy Agency (JAEA), 1-1-1 Kouto, Sayo-cho, Sayo-gun, Hyogo, 679-5148, Japan

Supporting Information

ABSTRACT: We synthesized two high-pressure polymorphs $PbNiO_3$ with different structures, a perovskite-type and a $LiNbO_3$-type structure, and investigated their formation behavior, detailed structure, structural transformation, thermal stability, valence state of cations, and magnetic and electronic properties. A perovskite-type $PbNiO_3$ synthesized at 800 °C under a pressure of 3 GPa crystallizes as an orthorhombic $GdFeO_3$-type structure with a space group *Pnma*. The reaction under high pressure was monitored by an in situ energy dispersive X-ray diffraction experiment, which revealed that a perovskit-type phase was formed even at 400 °C under 3 GPa. The obtained perovskite-type phase irreversibly transforms to a $LiNbO_3$-type phase with an acentric space group *R3c* by heat treatment at ambient pressure. The Rietveld structural refinement using synchrotron X-ray diffraction data and the XPS measurement for both the perovskite- and the $LiNbO_3$-type phases reveal that both phases possess the valence state of $Pb^{4+}Ni^{2+}O_3$. Perovskite-type $PbNiO_3$ is the first example of the $Pb^{4+}M^{2+}O_3$ series, and the first example of the perovskite containing a tetravalent A-site cation without lone pair electrons. The magnetic susceptibility measurement shows that the perovskite- and $LiNbO_3$-type $PbNiO_3$ undergo antiferromagnetic transition at 225 and 205 K, respectively. Both the perovskite- and $LiNbO_3$-type phases exhibit semiconducting behavior.

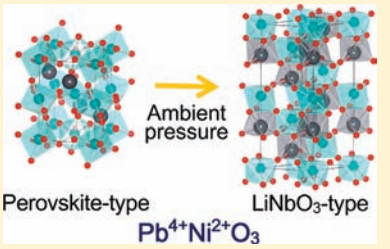

INTRODUCTION

Perovskite (Pv)-type oxides (general formula: ABO_3) have attracted widespread scientific and technological interest for several decades due to their various functional properties. Because the $LiNbO_3$ (lithium niobate, LN)-type structure is closely related to the Pv-type one, it is expected that LN-type oxides[1] would exhibit attractive functional properties like those of Pv-type oxides. Indeed, two of the well-known LN-type oxides, $LiNbO_3$ and $LiTaO_3$,[2] exhibit excellent polar properties such as ferroelectricity, piezoelectricity, and pyroelectricity based on their noncentrosymmetric structure[3] and have been extensively investigated from both a fundamental and a technological perspective. However, studies on functional LN-type oxides have been limited due to the small number of these oxides that can be synthesized at atmospheric pressure. To the best of our knowledge, $LiNbO_3$, $LiTaO_3$, $LiReO_3$,[4] $Li_{1-x}Cu_xNbO_3$,[5] and $(Li,Cu)TaO_3$[6] are the only LN-type oxides that have been synthesized at ambient pressure. On the other hand, in the field of earth science, the LN-type phase is considered to be an unquenchable high-pressure Pv-type phase, and several LN-type phases have been reported as metastable quenched phases.[1] To date, LN-type oxides such as $MnMO_3$ (M = Ti,[7−10] Sn[11,12]), $FeMO_3$ (M = Ti,[8,12−14] Ge[15]), $MgMO_3$ (M = Ti,[16] Ge[8,17,18]), $ZnGeO_3$,[18,19] garnet,[20] and $CuTaO_3$[21] have been stabilized by high-pressure and high-temperature heat treatment. Syono et al.[7,11] and Sleight et al.[21] first have investigated the functional properties of LN-type oxides synthesized under high pressure. On the basis of their findings, it is anticipated that functional LN-type oxides could be obtained by high-pressure synthesis. In fact, we have recently found that LN-type $ZnSnO_3$, which is a polar oxide with a noncetrosymmetric space group *R3c*, can be synthesized under high pressure.[22] Furthermore, in LN-type $MnMO_3$ (M = Ti, Sn) synthesized at high pressure, anomalies in the dielectric permittivity were observed at the weak ferromagnetic transition temperature, indicating the correlation between magnetic and dielectric properties.[23] Recently, we have synthesized a $GdFeO_3$-type orthorhombic perovskite $PbNiO_3$ under a pressure of 3 GPa and found that the Pv-type phase transforms to the LN-type phase by a heat treatment at 400−500 K under ambient pressure,[24] resulting in two metastable polymorphs of $PbNiO_3$ at atmospheric pressure. This is the first case in which both the Pv-type and the LN-type phases

Received: July 6, 2011
Published: September 04, 2011

dx.doi.org/10.1021/ja206247j | *J. Am. Chem. Soc.* 2011, 133, 16920–16929

were available at ambient pressure. Therefore, elucidation of the synthesis, structures, structural transformation, and physical properties of these two phases, as well as a comparison between them, would strongly contribute to the research field of chemistry and earth science.

In this study, therefore, we prepared the Pv-type and LN-type $PbNiO_3$ phases and investigated their formation, detailed structures, thermal stability, valence states, and magnetic and electronic properties. On the basis of the results, we discuss the structural transformation and structure−property relations of these different structure types.

EXPERIMENTAL PROCEDURES

Polycrystalline perovskite-type $PbNiO_3$ (abbreviated as Pv-PNO below) was synthesized by a solid-state reaction under high pressure at elevated temperature. The mixture of stoichiometric amounts of rutile-type β-PbO_2 (purity >99.999%) and NaCl-type NiO (purity > 99.9%) powder was allowed to react in a TRY cubic multianvil-type high-pressure apparatus (NAMO 2001) at 3 GPa and 1073 K (800 °C) for 1 h, and then was quenched to room temperature followed by the release of the pressure. The experimental details on the high-pressure synthesis of a Pv-type $PbNiO_3$ are available in the Supporting Information. To monitor the reaction between PbO_2 and NiO to form the Pv-PNO under high pressure, in situ energy dispersive synchrotron X-ray diffraction experiments were performed using a multianvil-type high-pressure apparatus SMAP2 installed in beamline BL14B1 at SPring-8 in Hyogo, Japan.[25] White X-rays with an energy of 20−160 keV from a bending magnet source were used as the incident X-rays. The diffraction data were collected by a Ge solid-state detector mounted on a goniometer at the fixed diffraction angles 2θ of 3.2° or 3.3° and 4.3° or 4.4°. The diffraction spectra of the samples were collected in the energy range of 60−90 keV, where the absorption of X-rays by the Au sample capsule was relatively low. The assembly of pressure cell was the same as that for high-pressure synthesis.

The $LiNbO_3$-type $PbNiO_3$ (abbreviated as LN-PNO below) powder was obtained by heating the powder of Pv-PNO at 523 K for 40 h with an intermediate grinding. The phase identification of the obtained samples was performed by the X-ray powder diffraction (XRD) method using a Rigaku RINT2100 diffractometer (graphite-monochromatized Cu Kα). To investigate the phase transformation, the high-temperature X-ray diffraction measurement was done in the temperature range of 300−923 K using the same diffractometer equipped with a heater attachment. The thermogravimetry differential thermal analysis (TG-DTA) was carried out using a Bruker AXS (Mac Science) TG-DTA2020S thermal analyzer to evaluate the thermal stability of $PbNiO_3$. The measurement was done in the temperature range of 300−1080 K upon heating at a rate of 10 K/min. Synchrotron powder XRD data at room temperature were collected on a Debye−Sherrer-type powder diffractometer with an imaging plate-type detector installed in the beamline BL02B2 at SPring-8. The scan step size was 0.01° in 2θ at a wavelength of λ = 0.51910 Å for Pv-PNO and 0.52035 Å for LN-PNO. Here, the sample was packed into a glass capillary of 0.1 mm diameter for Pv-PNO and 0.2 mm diameter for LN-PNO. The crystal structure was refined using the Rietveld analysis program, RIETAN-FP.[26] The crystal structures were drawn using the program VESTA[27] based on the structural refinement results. The Madelung energy calculation was done using the program MADEL developed by Dr. Kato, which is embedded in VESTA. The X-ray photoelectron spectroscopy (XPS) spectra were recorded using an ULVAC PHI Quantum 2000 spectrometer with Al Kα radiation. The bulk sample was set in the high-vacuum chamber. The surface of the sample was then sputtered by the Ar-ion beam (the acceleration voltage was 2 kV) to obtain a clean surface. The cleanness was checked by the disappearance of the C1s peak originated from adsorbed carbon dioxide.

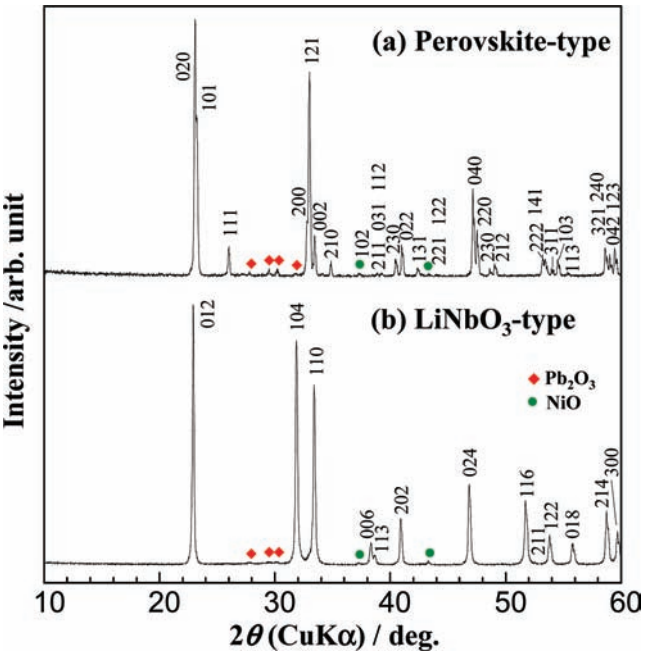

Figure 1. Laboratory powder X-ray diffraction patterns for the perovskite-type $PbNiO_3$ (a) and $LiNbO_3$-type $PbNiO_3$ (b) at room temperature.

The neutrizer was used after sputtering to avoid the charging up of the sample. The diameter of the X-ray beam was 50 μm. The acceleration voltage was 15 kV. The data were collected in the range of 130−150 eV and 840−890 eV with 0.1 eV steps for Pb 4f and Ni 2p, respectively.

The temperature dependence of the dc magnetic susceptibility (χ) and magnetic field dependence of isothermal magnetization were measured under a magnetic field of 0.01−1 T using a SQUID magnetometer (Quantum Design MPMS System) in the temperature range of 5−300 K. The samples were cooled in the zero-field or under a magnetic field, and the susceptibilities were recorded continuously upon heating. The electronic resistivities of the samples were measured in the temperature range of 7−330 K by a conventional four-probe method. Here, for Pv-PNO, the bulk sample synthesized at high pressure was used as the specimen. On the other hand, to obtain the bulk specimen for LN-PNO, LN-PNO powder was sintered under a condition of 3 GPa and 300 °C for 1 h. It was then confirmed that LN-PNO was not transformed into Pv-PNO.

RESULTS AND DISCUSSION

High-Pressure Synthesis and Formation Behavior of Perovskite-type $PbNiO_3$. The color of the as-synthesized powder under high pressure was dark gray. The XRD pattern (Figure 1a) showed that the as-synthesized sample was an orthorhombic perovskite-type phase (Pv-PNO) with small residual amounts of NiO and Pb_2O_3. In situ energy dispersive XRD patterns for the formation of Pv-PNO under high-pressure and high-temperature conditions are shown in Figure 2. The diffraction peaks as well as Pb Kα X-ray fluorescence lines originated from the samples can be observed in their patterns. The compression up to 3 GPa at room temperature resulted in the broadening of diffraction peaks for the starting materials, PbO_2 and NiO, as well as the compression of the lattice of these compounds (Figure 2a and b). A possible mechanism responsible for the peak broadening is the deformation related to the microscopic strain due to non-hydrostatic conditions.[28,29]

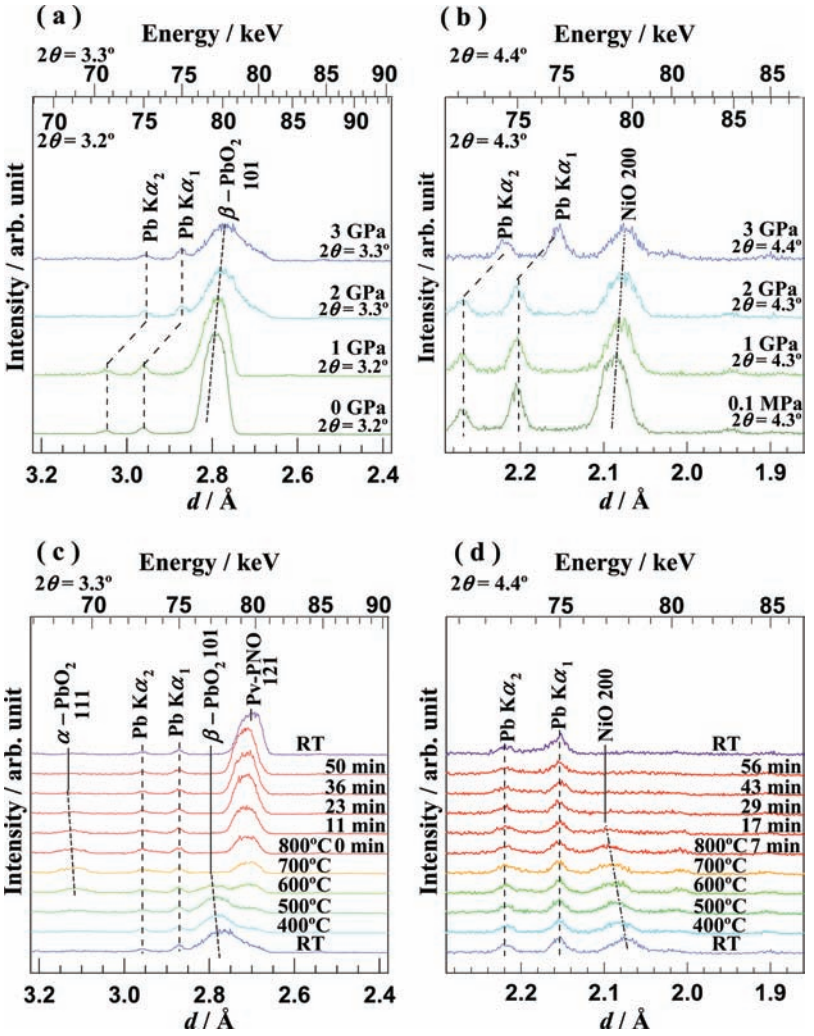

Figure 2. In situ X-ray diffraction (XRD) patterns for the formation of the perovskite-type $PbNiO_3$ (Pv-PNO): the variation of XRD patterns versus pressure at room temperature with respect to PbO_2 (a) and NiO (b), the series of XRD patterns for the formation of Pv-PNO (c) and (d).

As shown in Figure 2c, the formation of Pv-PNO began at a temperature as low as 400 °C. As the temperature was elevated, the formation of Pv-PNO was promoted along with the consumption of PbO_2 and NiO, and the reaction was almost completed at 800 °C (Figure 2c and d). In addition, the phase transformation of rutile-type β-PbO_2 to orthorhombic α-PbO_2 was clearly observed at 600 °C (Figure 2c), which is consistent with the report by Yagi et al.[30] It is not likely that the phase transformation of PbO_2 strongly influenced the formation of Pv-PNO. After the decrease in temperature and release of pressure, the Pv-type phase was sustained and quenched. Consequently, no transformation to the LN-type phase was observed during the high-pressure and heat treatment. At the end of the next section, we will discuss the quenching of the perovskite form in the high-pressure synthesis.

Structural Transformation, Thermal Stability, and Valence States of Perovskite-type and $LiNbO_3$-type $PbNiO_3$. By heat treatment of the Pv-PNO at 523 K for 40 h with intermediate grinding, the structural transformation to the LN-PNO could be realized. The powder XRD pattern of LN-PNO is shown in Figure 1b. The distinct change in color was not recognized. The transformation was irreversible, and the LN-PNO remained after the temperature decreased to room temperature, indicating that the LN-PNO is thermodynamically more stable than the Pv-PNO at ambient pressure. Ross et al. have reported that LN-type $MnTiO_3$ reversibly transforms directly to an orthorhombic Pv-type phase between 2 and 3 GPa.[10] This supports that the LN-type phase is more stable than the Pv-type phase at ambient pressure. Figure 3 shows the variation of the powder XRD patterns with increasing temperature from 300 to 873 K for the Pv-PNO in the ambient atmosphere. As shown in Figure 3, the LN-type phase appeared even at 423 K, and the Pv-PNO gradually transformed to the LN-PNO with increasing temperature. At 823 K, the partial decomposition was observed, and at 873 K the whole sample decomposed into PbO and NiO.

Figure 4 shows the results of TG-DTA for the Pv-PNO sample. As seen in Figure 4, a decrease in weight accompanied by an endothermal peak was observed. The identification by XRD revealed that the sample after the measurement was a mixture of PbO and NiO. The weight loss by 5% and endothermal process can be explained by the evolution of oxygen gas accompanied by the decomposition reaction: $PbNiO_3 \rightarrow PbO + NiO + 1/2O_2$. The finding is consistent with the results of the

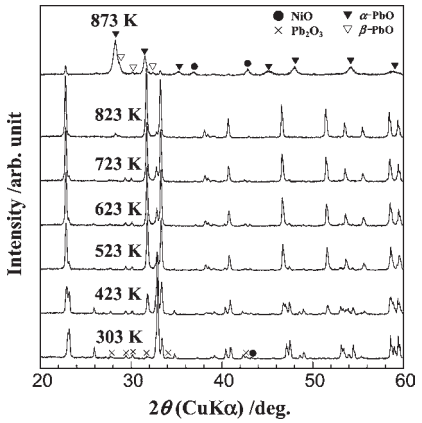

Figure 3. Variation of the powder X-ray diffraction patterns with increasing temperature from 300 to 873 K for the perovskite-type $PbNiO_3$ at ambient atmosphere.

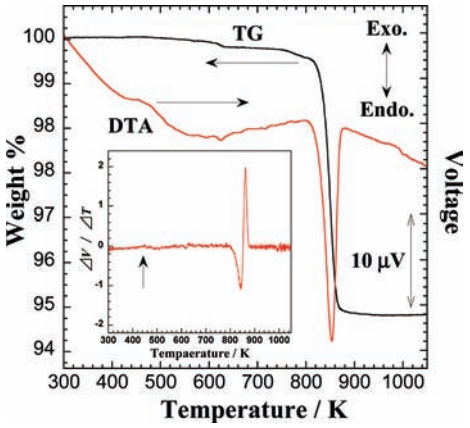

Figure 4. The response of the thermogravimetry and differential thermal analysis (TG-DTA) for the perovskite-type $PbNiO_3$ sample. The inset shows the derivative curve of the DTA signal with respect to temperature.

high-temperature XRD experiment. Furthermore, an exothermal broad cusp can be observed in the vicinity of 450 K as seen in Figure 4. A change in the derivative of the DTA signal with respect to temperature was also detected in the same temperature region, as shown in the inset of Figure 4. This anomaly probably corresponds to the transformation from the Pv-PNO to the LN-PNO. We will discuss the thermal behavior later.

The observed and calculated synchrotron XRD patterns from the Rietveld analysis for the Pv-PNO and the LN-PNO at room temperature are shown in Figure 5a and b, respectively. When the Rietveld refinements were performed assuming a $GdFeO_3$-type perovskite structure with a centrosymmetric space group *Pnma* (No. 62) for the Pv-PNO, and a hexagonal polar $LiNbO_3$-type structure with an acentric space group *R*3*c* (No. 161) for the LN-PNO, good results were obtained. Nishiyama and Hayashi[31] have reported that an orthorhombic perovskite $NiPbO_3$ can be synthesized under a pressure of 5 GPa at 1000 °C, but they considered that Ni ion is accommodated into the A-site of the perovskite. On the other hand, the structural refinement in our study revealed that Pb ion occupies the A-site and Ni ion occupies the B-site for the Pv-type phase, that is, $PbNiO_3$. The refined structural parameters by the Rietveld analysis for the Pv-PNO and the LN-PNO are summarized in Tables 1 and 2, respectively. The selected

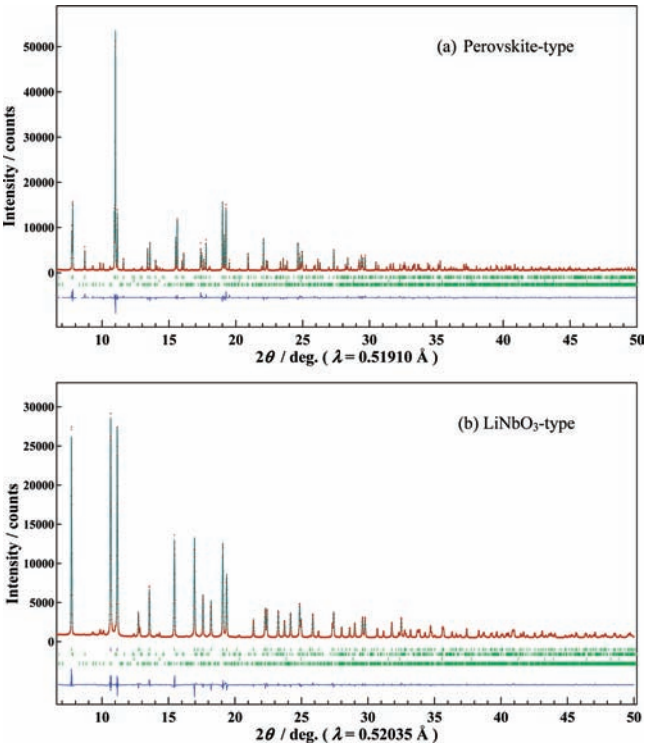

Figure 5. Observed and calculated synchrotron X-ray diffraction patterns from the Rietveld analysis for the perovskite-type $PbNiO_3$(a) and $LiNbO_3$-type $PbNiO_3$ (b) at room temperature.

Table 1. Structural Parameters for a Perovskite-type $PbNiO_3$[a]

atom	site	*g*	*x*	*y*	*z*	*B*/Å^2
Pb	4c	1.0	0.45829(9)	0.25	0.00761(18)	0.281(11)
Ni	4a	1.0	0	0	0	1.50(3)
O1	4c	1.0	0.593(2)	0.25	0.6236(19)	2.0
O2	8d	1.0	0.1846(16)	0.0748(10)	0.3192(15)	2.0

[a] Space group: *Pnma* (No .62), $Z = 4$. Lattice parameters (orthorhombic): $a = 5.46325(4)$ Å, $b = 7.70741(5)$ Å, $c = 5.35827(4)$ Å. $R_{wp} = 5.56\%$, $R_p = 4.04\%$, $R_e = 3.30\%$, $S = 1.68$, $R_I = 3.03\%$, $R_F = 1.71\%$. *B* values for O are fixed to 2.0 Å^2. Uncertainties are shown in parentheses, following the last significant figures to which they are attributed.

interatomic distances and angles, bond valence sum (BVS),[32−35] and Madelung energy for both phases are summarized in Table 3. The crystal structures for both phases are also shown in Figure 6.

The estimated BVS from the interatomic distances indicates that both phases possess the valence state of $Pb^{4+}Ni^{2+}O_3$. This is supported by the XPS experiments. The Pb 4f and Ni 2p core-level spectra for both Pv-PNO and LN-PNO are shown in Figure 7a and b, respectively. The $Pb4f_{7/2}$ and the Ni $2p_{3/2}$ binding energies for Pv-PNO and LN-PNO were summarized with the reference data for β-PbO_2, PbO, and NiO in Table 4. As seen in Table 4, the $Pb4f_{7/2}$ binding energies for Pv-PNO and LN-PNO are close to those for PbO_2, rather than those for PbO; that is, the valence of Pb is 4+ rather than 2+. Furthermore, the Ni $2p_{3/2}$ binding energies for Pv-PNO and LN-PNO are close to that for NiO,[36] indicating that the valence of Ni for PNO is 2+.

There have been several reports on Pv-type oxides with a valence state of $A^{4+}B^{2+}O_3$, that is, containing divalent ions at the B-site

dx.doi.org/10.1021/ja206247j |*J. Am. Chem. Soc.* 2011, 133, 16920–16929

Table 2. Structural Parameters for a $LiNbO_3$-type $PbNiO_3$[a]

atom	site	g	x	y	z	B/Å^2
Pb	6a	1.0	0	0	0.28641(8)	0.599(9)
Ni	6a	1.0	0	0	0	0.73(2)
O	18b	1.0	0.0487(11)	0.3657(9)	0.0668(9)	1.02(9)

[a] Space group: $R3c$ (No. 161), Z = 6. Lattice parameters (hexagonal): a = 5.36268(8) Å, c = 14.09038(12) Å. R_{wp} = 3.85%, R_p = 2.85%, R_e = 3.11%, S = 1.24, R_I = 0.92%, R_F = 0.41%. Uncertainties are shown in parentheses, following the last significant figures to which they are attributed.

Table 3. Selected Interatomic Distances (Å), Bond Angles (deg), and Calculated Bond Valence Sum (BVS) of Cations at Room Temperature for a Perovskite-type $PbNiO_3$ and a $LiNbO_3$-type $PbNiO_3$

	perovskite-type	$LiNbO_3$-type
	Distance/Å	
Ni−O1	2.100(4) × 2	2.109(6) × 3
		2.071(6) × 3
Ni−O2	2.068(8) × 2	
	2.059(8) × 2	
average Ni−O	2.076	2.090
distortion Δ of NiO_6	7.185×10^{-5}	8.264×10^{-5}
Pb−O1	2.185(10) × 1	2.246(6) × 3
	2.116(12) × 1	2.104(6) × 3
Pb−O2	2.810(8) × 2	
	2.617(8) × 2	
	2.053(8) × 2	
average Pb−O	2.407	2.175
distortion Δ of PbO_6		1.066×10^{-3}
	Bond Angle/deg	
Ni−O1−Ni	133.1(3)	136.7(2)
Ni−O2−Ni	136.0 (2)	
	BVS	
atom (assumed valence)	BVS (deviation from assumed valence)	BVS (deviation from assumed valence)
Pb (+4)	4.11 (+3%)	4.27 (+7%)
Ni (+2)	1.92 (−4%)	1.85 (−8%)
Madelung energy	-1.684×10^4 kJ/mol	-1.694×10^4 kJ/mol

positions. Among them, the Pv-type oxides, $Se^{4+}M^{2+}O_3$ and $Te^{4+}M^{2+}O_3$, with M = Mg, Mn, Co, Ni, Cu, and Zn,[37−40] have been synthesized under high-pressure and high-temperature conditions. Recently, Ishiwata et al. found a +4−+2 valence state for A−B in a perovskite $(Bi_{0.8}Pb_{0.2})NiO_3$.[41] Because their $A^{4+}B^{2+}O_3$ perovskites contain tetravalent cations with an electronic configuration of ns^2, that is, lone pair electrons, at the A positions (Se^{4+}, Te^{4+}, Bi^{3+}, Pb^{2+}), it is thought that the lone pair electrons should be crucial for the stabilization of $A^{4+}B^{2+}O_3$ perovskite.[39−41] On the other hand, in $PbNiO_3$, because Pb^{4+} has the electronic configuration of $5d^{10}6s^0$, the stabilization of the valence state of $A^{4+}B^{2+}O_3$ due to the lone pair is ruled out. The distortions of NiO_6 octahedra for both Pv- and LN-PNO as estimated by the formula[32]

$$\Delta = \frac{1}{6}\sum_{i=1}^{6}\left(\frac{d_i - d_{av}}{d_{av}}\right)^2$$

(where d_i is the individual Ni−O bond distance and d_{av} is the average bond distance) are close, $\Delta = 7.2 \times 10^{-5}$ and 8.3×10^{-5}, respectively, which are quite a good deal smaller than those for other Ni^{2+}-containing perovskites: for example, $\Delta = 3 \times 10^{-4}$ for $SeNiO_3$[39] or $\Delta = 18 \times 10^{-4}$ for $(Bi_{0.8}Pb_{0.2})NiO_3$.[41] The large distortion of NiO_6 octahedra in $SeNiO_3$ and $(Bi_{0.8}Pb_{0.2})NiO_3$ is due to the strong covalency of the A−O bond and/or the steric effect by the lone pair electron (ns^2).[39−41] The smaller distortion in $PbNiO_3$ indicates that their influences are relatively small, which is attributed to the electronic configuration of $Pb^{4+}(d^{10}s^0)$ without lone pair electrons. Furthermore, among the known perovskite-type $PbMO_3$ compounds (M = transition metal ion: Ti,[42,43] V,[44−46] Cr,[47−50] Mn,[51] Fe,[52] Ru[53−55]), $PbMO_3$ (M = Ti, V, Cr, Mn, Ru) exhibits the valence state of $Pb^{2+}M^{4+}O_3$, and in $PbFeO_3$, the Fe is trivalent and the disproportionation of Pb (Pb^{2+} and Pb^{4+}) occurs. $PbNiO_3$ is therefore the first case of a $Pb^{4+}M^{2+}O_3$ perovskite. On the basis of these results, the stability of the valence state of $Pb^{4+}Ni^{2+}O_3$ is likely to be related to the electronic structure of Ni^{2+} at the octahedral site. Because the Ni^{2+} ion with a high spin state in octahedral coordination ($3d^8$, $t_{2g}^6e_g^2$) exhibits the highest crystal field stabilization energy (CFSE) among the divalent 3d transition metal ions,[56] the high CFSE of Ni^{2+} at the NiO_6 octahedron helps to stabilize Ni^{2+}-containing Pv- and LN-type oxides.[24]

Here again, we will discuss the structural transformation on the basis of the structural information. The Pv-PNO and LN-PNO are close in that the NiO_6 octahedra share their corners three-dimensionally, as shown in Figure 6. First, we compare the pseudocubic primitive cells (subcells) including a formula unit of $PbNiO_3$ for both phases. The relationship between the subcells and the true cells[57] is schematically shown in the middle of Figure 6. Actually, for Pv-PNO, the subcell is a monoclinic one with $a_m = c_m$ = 3.826 Å, b_m = 3.854 Å, β = 91.11°. The relation between the orthorhombic unit cell vectors, $\mathbf{a}_{ortho}$, $\mathbf{b}_{ortho}$, $\mathbf{c}_{ortho}$, and the monoclinic subcell vectors, $\mathbf{a}_m$, $\mathbf{b}_m$, $\mathbf{c}_m$, is given by:

$$\mathbf{a}_{ortho} = \mathbf{a}_m - \mathbf{c}_m,\ \mathbf{b}_{ortho} = 2\mathbf{b}_m,\ \mathbf{c}_{ortho} = \mathbf{a}_m + \mathbf{c}_m$$

and the matrix representation is as follows:

$$\begin{pmatrix}\mathbf{a}_{ortho}\\ \mathbf{b}_{ortho}\\ \mathbf{c}_{ortho}\end{pmatrix} = \begin{pmatrix}1 & 0 & -1\\ 0 & 2 & 0\\ 1 & 0 & 1\end{pmatrix}\begin{pmatrix}\mathbf{a}_m\\ \mathbf{b}_m\\ \mathbf{c}_m\end{pmatrix}$$

It should be noted that b_m is greater than a_m, while typical $GdFeO_3$-type perovskites with the space group *Pnma* possess a_m greater than b_m, for example, a_m = 3.826 Å, b_m = 3.820 Å in $CaTiO_3$[58] and a_m = 3.932 Å, b_m = 3.927 Å in $LaFeO_3$.[59] On the other hand, for LN-PNO the subcell is a rhombohedral one with a_r = 3.886 Å, α = 87.26°. The relation between the hexagonal unit cell vectors, $\mathbf{a}_h$, $\mathbf{b}_h$, $\mathbf{c}_h$, and the rhombohedral subcell vectors, $\mathbf{a}_r$, $\mathbf{b}_r$, $\mathbf{c}_r$, is given by:

$$\mathbf{a}_h = \mathbf{a}_r - \mathbf{b}_r,\ \mathbf{b}_h = \mathbf{b}_r - \mathbf{c}_r,\ \mathbf{c}_h = 2(\mathbf{a}_r + \mathbf{b}_r + \mathbf{c}_r)$$

and the matrix representation is as follows:

$$\begin{pmatrix}\mathbf{a}_h\\ \mathbf{b}_h\\ \mathbf{c}_h\end{pmatrix} = \begin{pmatrix}1 & -1 & 0\\ 0 & 1 & -1\\ 2 & 2 & 2\end{pmatrix}\begin{pmatrix}\mathbf{a}_r\\ \mathbf{b}_r\\ \mathbf{c}_r\end{pmatrix}$$

The transformation from Pv-PNO to LN-PNO induces the change from the monoclinic distortion parallel to the [101]

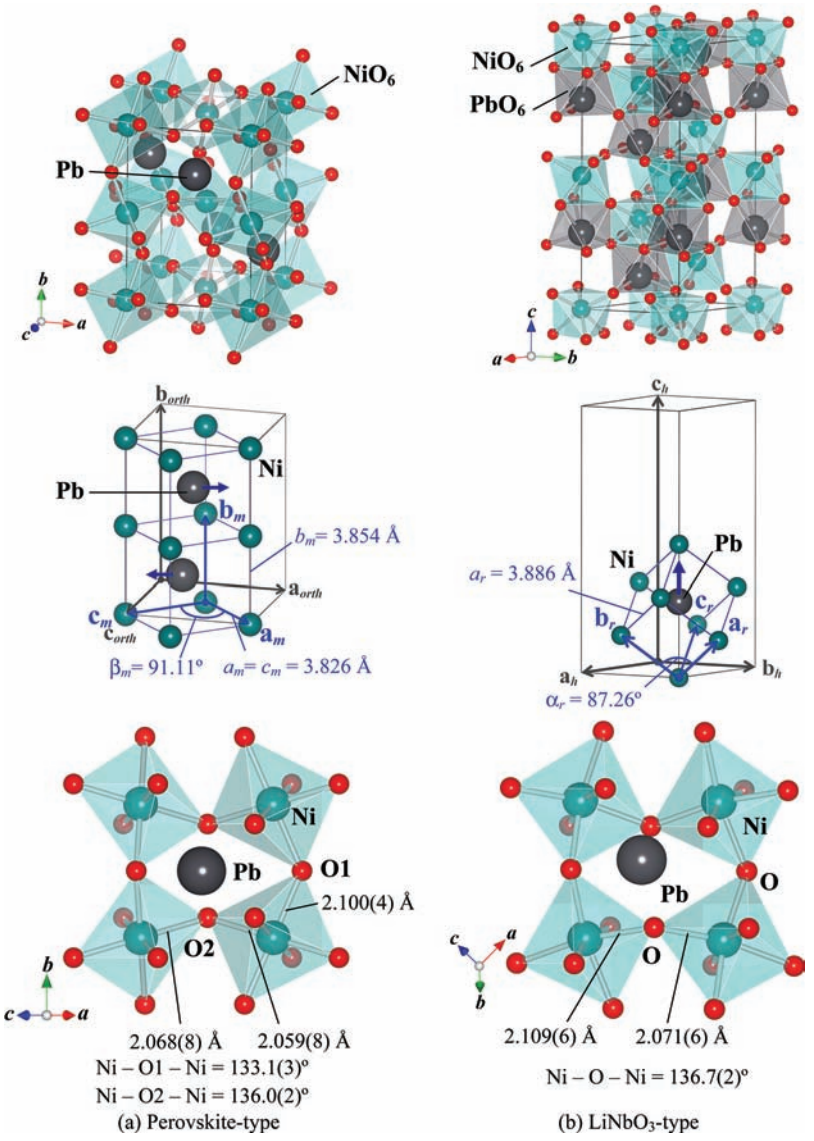

Figure 6. Crystal structures for the perovskite-type $PbNiO_3$ (a) and $LiNbO_3$-type $PbNiO_3$ (b).

direction of subcell to the rhombohedral one parallel to the [111] direction of subcell accompanied by an increase in the lattice volume.

Next, we compare the manner of tilting of the NiO_6 octahedra and the location of the Pb ion. For Pv-PNO with the space group of *Pnma*, the out-of-phase tilt along the [100] and [001] directions of the subcell and in-phase tilt along the [010] direction of subcell occur (tilting system, Glazer notation,[60,61] $a^-b^+a^-$). In addition, the Pb ion is displaced along the approximate $[\bar{1}01]$ or $[10\bar{1}]$ direction of the subcell (the approximate $[\bar{1}00]$ or [100] directions of the orthorhombic cell) in antiparallel sheets perpendicular to [010] just as in the case of the $GdFeO_3$-type $CaTiO_3$,[61] which doubles the cell length along the [010] direction. As a result, Pv-PNO possesses an orthorhombic unit cell of $\sim\sqrt{2}a_p \times \sim 2a_p \times \sim\sqrt{2}a_p$ ($2a_m \sin(\beta_m/2) \times 2b_m \times 2a_m \cos(\beta_m/2)$). Here, a_p is the pseudocubic subcell length. On the other hand, in LN-PNO with the space group of *R*3*c*, an out-of-phase tilt along all the directions of the subcell occurs (tilting system, Glazer notation, $a^-a^-a^-$). Furthermore, all of the Pb ions are displaced simultaneously along the [111] direction of the subcell (the [001] directions of the hexagonal cell). As a result, LN-PNO possesses a hexagonal unit cell of $\sim\sqrt{2}a_p \times \sim\sqrt{2}a_p \times \sim 2\sqrt{3}a_p$ ($2a_r \sin(\alpha_r/2) \times 2a_r \sin(\alpha_r/2) \times 2\sqrt{3}a_r\sqrt{(3-4\sin(\alpha_r/2)^2)}$). Although the Pb ion is coordinated by eight oxygens for Pv-PNO, it should be noted that the Pb atom is primarily surrounded by four oxygens at 2.1−2.2 Å, with an additional four oxygens at 2.6−2.8 Å as seen in Table 3. The distinct difference between the bond distances of A−O in $GdFeO_3$-type perovskites can be normally observed due to the displacement of the A-site ion within A-site cage; for example, the bond distances are 2.4−2.7 Å in $CaTiO_3$[58] and 2.4−2.8 Å in $LaFeO_3$.[59] However, the difference of 0.7 Å in Pv-PNO is much greater than those of typical $GdFeO_3$-type perovskites. On the other hand, in the fluorite-type PbO_2,[62] the tetravalent Pb ion is equidistantly surrounded by eight oxygens at 2.316 Å. Here, the fluorite-type PbO_2 is one of the high-pressure phases of the rutile-type PbO_2 (β-PbO_2) in which the coordination number of Pb is six. As compared to the isotropic eight coordination in the fluorite-type PbO_2, the anisotropic 4 + 4 coordination in Pv-PNO stands marginally in the regime of the conventional high-pressure chemistry where the coordination number increases with increasing pressures.

dx.doi.org/10.1021/ja206247j |*J. Am. Chem. Soc.* 2011, 133, 16920–16929

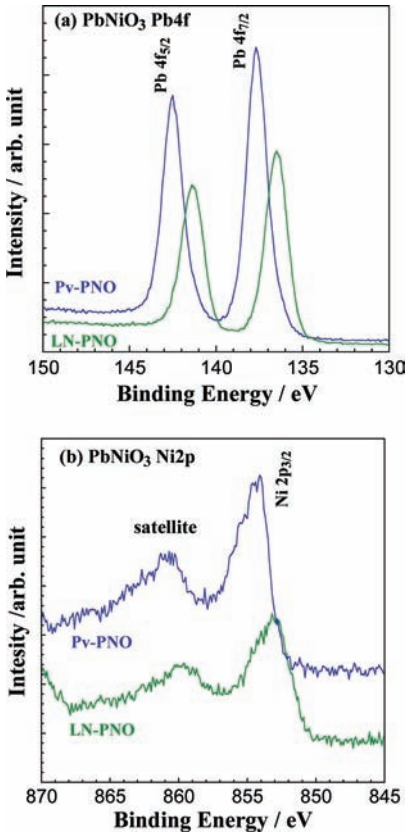

Figure 7. Pb 4f (a) and Ni 2p (b) core-level spectra for the perovskite-type $PbNiO_3$ (Pv-PNO) and $LiNbO_3$-type $PbNiO_3$ (LN-PNO).

Table 4. Binding Energies (BE) of Pb $4f_{7/2}$ Electrons and Ni $2p_{3/2}$ Electrons for a Perovskite-type $PbNiO_3$ (Pv-PNO) and a $LiNbO_3$-type $PbNiO_3$ (LN-PNO) with the Reference Data for β-PbO_2, PbO, and NiO

material	BE of Pb $4f_{7/2}$ (eV)	BE of Ni $2p_{3/2}$ (eV)	reference
Pv-PNO	137.7	854.2	this work
LN-PNO	136.5	853.1	this work
β-PbO_2	137.5		36
	137.6		37
PbO	137.9		36
	138.2		37
NiO		853.7	38

The Pb ion for the LN-PNO is coordinated by six oxygens at 2.10 and 2.25 Å, which is close to the reported Pb−O distances which the tetravalent Pb in octahedral coordination takes, for example, 2.12, 2.18, and 2.22 Å in α-PbO_2,[63] 2.15 and 2.17 Å in β-PbO_2,[64] 2.14 and 2.15 Å in Ba_2PbO_4[65] with K_2NiF_4 structure, and 2.1 and 2.2 Å in the zeolite in which Pb exists both in +2 and in +4 oxidation states.[66]

The transformation from the Pv-PNO to the LN-PNO can be attained by the tilting of NiO_6 octahedra and the displacement of the Pb ion without a long-range diffusion of constituent ions, which realizes the structure transformation at a rather low temperature of 400 K.

When we compare the lattice volume per formula unit (f.u.) estimated from the lattice parameters, the order of the values is as follows: 56.2 $Å^3$/f.u. for Pv-PNO, 58.4 $Å^3$/f.u. for LN-PNO, and the sum (59.9 $Å^3$/f.u.) of 41.6 $Å^3$/f.u. for the rutile-type β-PbO_2[64] and 18.2 $Å^3$/f.u. for the NaCl-type NiO.[67] These data are consistent with the fact that the Pv-type phase was stabilized by high-pressure synthesis and transformed to the LN-PNO after heat treatment at ambient atmosphere; that is, the Pv-type phase is the high-pressure phase of the LN-type phase in $PbNiO_3$ the same as in $MnTiO_3$,[10] which is supported by the finding that the absolute value of Madelung energy for LN-PNO is greater than that for Pv-PNO, as seen in Table 3. Exothermal heat corresponding to the transformation from Pv-PNO to LN-PNO is expected from the calculated Madelung energy. This finding supports the idea that the exothermal broad cusp in the vicinity of 450 K in the DTA signal (Figure 4) corresponds to the transformation from Pv-PNO to LN-PNO. On the basis of these results, we anticipate that the transformation from the Pv-type phase to the LN-type phase would be related to the small difference in the lattice energy for both compounds as well as the similarity of their structures. More quantitative thermal analyses will be done to elucidate the thermodynamics of Pv-PNO and LN-PNO.

Finally, we will discuss the quenching of the perovskite form in the high-pressure synthesis. The in situ X-ray diffraction experiment indicated that the Pv-PNO phase is stable at 3 GPa and 800 °C. On the other hand, when LN-PNO was annealed at 3 GPa and 300 °C for 1 h, we confirmed that the LN-type phase was obtained without the transformation to the Pv-type phase. We can therefore expect that the LN-PNO would be thermodynamically more stable than Pv-PNO at 3 GPa and at least up to 300 °C, and LN-PNO would be obtained in the cooling process in the high-pressure synthesis. However, we were able to obtain the Pv-PNO without the transformation to LN-PNO. The possible explanations for this phenomenon are as follows. One predominant factor is the kinetics of the transformation, that is, diffusion for ions. The cooling rate is too fast to transform the Pv-type phase to the LN-type phase. At room temperature, the activation energy for diffusion is too high for the Pv-type phase to transform to the LN-type phase. Another factor is the change in lattice volume for the transformation. The lattice volume of LN-PNO is greater than that of Pv-PNO. When the Pv-PNO is transformed to the LN-PNO, the internal pressure in the sample cell increases with the increase in lattice volume accompanying the transformation. This effect also would suppress the phase transformation from Pv-PNO to LN-PNO in the cooling process.

Magnetic and Electrical Properties of $PbNiO_3$. Figure 8 shows the temperature dependence of magnetic susceptibilities measured under a magnetic field of 0.1 T in both the zero field cool (hereafter abbreviated as ZFC) and the field cool (hereafter abbreviated as FC) modes for the Pv-PNO and LN-PNO. As shown in Figure.8, the antiferromagnetic behaviors with peaks at 225 and 205 K were observed for Pv-PNO and LN-PNO, respectively. Because the antiferromagnetic interaction is strengthened by the superexchange interaction between Ni ions via oxygen, we can expect that the higher bond angle of Ni−O−Ni serves the higher antiferromagnetic transition temperature. However, the average bond angle of Pv-PNO is smaller than that of LN-PNO (see Table 3 and Figure 6). On the other hand, the magnetic interaction is also dependent on the interatomic distance between Ni and O. Therefore, the finding that the T_N for Pv-PNO is higher than that for LN-PNO is primarily attributable to the fact that the bond distance of Ni−O for

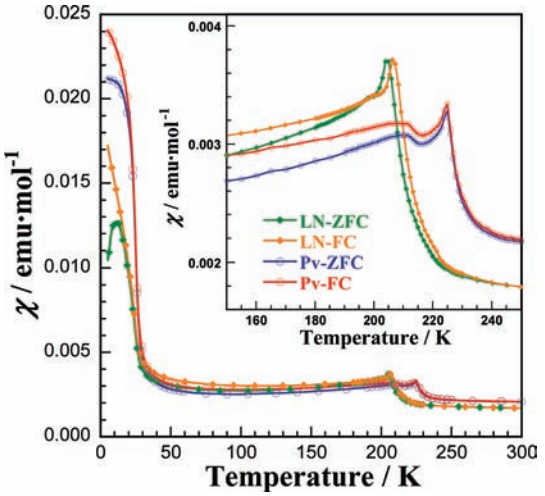

Figure 8. Temperature dependence of magnetic susceptibilities measured in an applied magnetic field of 0.1 T in both zero field cool (ZFC) and field cool (FC) modes for the perovskite-type $PbNiO_3$ (Pv-PNO) and $LiNbO_3$-type $PbNiO_3$ (LN-PNO).

Pv-PNO was smaller than that for LN-PNO. The magnetic susceptibility above T_N was fitted to the Curie−Weiss law, $\chi = C/(T - \theta_w)$. Here, C is the Curie constant and θ_w is the Weiss temperature. The calculated values are $C = 1.30 \pm 0.05$ and $\theta_w = -670 \pm 30$ K for Pv-PNO using the ZFC data from 260 to 300 K, and $C = 1.34 \pm 0.03$ and $\theta_w = -495 \pm 16$ K for LN-PNO using the ZFC data from 240 to 300 K. That the Weiss temperature in Pv-PNO was lower than that of LN-PNO indicates that the antiferromagnetic interaction between Ni ions via oxygen for Pv-PNO was stronger than that for LN-PNO, which is consistent with the finding of a greater Néel temperature for Pv-PNO than for LN-PNO. The effective magnetic moments were estimated to be $3.22 \pm 0.07\ \mu_B$ for Pv-PNO and $3.27 \pm 0.04\ \mu_B$ for LN-PNO, respectively. These values are close to the expected spin-only magnetic moment of Ni^{2+} with a high spin configuration ($S = 1$), $2.83\ \mu_B$. The discrepancy is thought to be due to the spin−orbit interaction. The isothermal magnetization curves (Figure S1 in the Supporting Information) were linear at 210 and 190 K just below T_N for Pv-PNO and LN-PNO, respectively, indicating that no canted ferromagnetism appeared accompanied by antiferromagnetic transition for both phases. Furthermore, below 30 K, the increase in magnetic susceptibility and the difference between ZFC and FC susceptibility were observed. As shown in Figure S1 in the Supporting Information, in the isothermal magnetization curve at 5 K, the hysteresis was observed for both Pv-PNO and LN-PNO, indicating that the increase in magnetic susceptibility below 30 K corresponds to the weak ferromagnetism. However, the magnetic susceptibility below 30 K and the magnetic moments estimated from the isothermal magnetization curve at 5 K (the order of 0.001 μ_B/Ni) were different between the prepared samples. Therefore, at the present time, we consider that the weak ferromagnetic behavior at low temperature was due to the small volume of magnetic impurity phases, although there is a possibility that the weak ferromagnetism was attributable to the canted spins with antiferromagnetic order at low temperature. The clarifications of the origin of the weak ferromagnetism and the magnetic structure remain for future study.

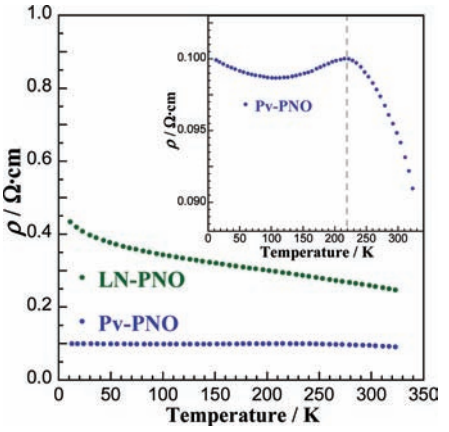

Figure 9. Temperature dependence of resistivities for the perovskite-type $PbNiO_3$ (Pv-PNO) and $LiNbO_3$-type $PbNiO_3$ (LN-PNO).

Although LN-PNO possesses a noncentrosymmetric (NCS) structure, as mentioned above, properties based on NCS structure were not evaluated due to the conductive behavior. Figure 9 shows the temperature dependence of resistivities for the Pv-PNO and LN-PNO. Both of the phases exhibited semiconducting behaviors with small temperature dependences of resistivity. The temperature dependence for LN-PNO was greater than that for Pv-PNO. The electronic conductivity of PNO is thought to originate from the orbital interaction between Ni3d and O2p, and/or the orbital interaction between Pb6s/6p and O2p, and the carrier due to oxygen nonstoichiometry. The magnetic behavior indicates that most of the d electrons for Ni ions are localized. Therefore, the semiconducting behavior for both compounds is primarily attributed to the orbital interaction between Pb 6s/6p and O2p and/or the electron carrier originated from the oxygen vacancy. The inset of Figure 9 shows an enlargement of resistivity for the Pv-PNO. As seen in this figure, the anomaly in resistivity was observed in the vicinity of 220 K, which is close to the Néel temperature. This finding indicates the partial contribution to the electronic property due to the orbital interaction between Ni3d and O2p, and the antiferromagnetic ordering of the 3d electrons of Ni ions in the Pv-PNO.

■ CONCLUSION

We obtained two high-pressure phases, a perovskite-type $PbNiO_3$ (Pv-PNO) and a $LiNbO_3$-type $PbNiO_3$ (LN-PNO), and elucidated the structural transformation, thermal stability, valence states of cations, and physical properties of the Pv-PNO and LN-PNO. In situ X-ray diffraction studies revealed that the Pv-PNO is formed without the transformation to LN-PNO under high temperature and pressure conditions. On the other hand, by the heat treatment of Pv-PNO at ambient atmosphere, the transformation from Pv-PNO to LN-PNO occurs irreversibly. The structural information by Rietveld refinement for both phases indicates that the transformation from Pv-PNO to LN-PNO occurs easily without a long-range diffusion of the constituent ions. The smaller lattice volume of Pv-PNO relative to LN-PNO implies that Pv-PNO is the high-pressure phase of LN-PNO. The structural analysis and the XPS measurement indicate that both the Pv-PNO and the LN-PNO possess a valence state of $Pb^{4+}Ni^{2+}O_3$. Pv-PNO is notable for the first example of the $Pb^{4+}M^{2+}O_3$ series, and the first example of the perovskite containing a 4+ A-site cation without lone pair electrons. The LN-PNO

and Pv-PNO with the valence state of $Pb^{4+}Ni^{2+}O_3$ are partly caused by the high crystal field stabilization energy of the Ni^{2+} ion in the octahedral site. The magnetic interaction of Ni^{2+} ions for both phases is antiferromagnetic, and the difference in the magnetic interaction between the Pv-PNO and the LN-PNO is dominated by the Ni−O distance rather than the Ni−O−Ni bond angles. Both phases exhibit semiconducting behavior.

■ ASSOCIATED CONTENT

Supporting Information. Experimental details on the high-pressure synthesis of a perovskite-type $PbNiO_3$. Isothermal magnetization curves are shown for the perovskite-type $PbNiO_3$ and the $LiNbO_3$-type $PbNiO_3$ at various temperatures. This material is available free of charge via the Internet at http://pubs.acs.org.

■ AUTHOR INFORMATION

Corresponding Author
yoshiyuki.inaguma@gakushuin.ac.jp

■ ACKNOWLEDGMENT

We thank Dr. H. Kojitani and Prof. M. Akaogi for their helpful input regarding the high-pressure synthesis. We are grateful to the reviewers for their useful advice and helpful comments. The work on the in situ synchrotron XRD measurements at high temperature and high pressure was performed under the Common-Use Facility Program of JAEA. The synchrotron powder XRD measurements at ambient pressure were carried out under the Priority Nanotechnology Support Program administered by the Japan Synchrotron Radiation Research Institute (JASRI) (proposal no. 2010A1669). This work was supported by a Grant-in-Aid for Scientific Research (no. 21360325) of the Japan Society for the Promotion of Science, the "High-Technology Research Center Project", and the Promotional Project for Development of a Strategic Research Base for Private Universities: Matching Fund Subsidies of the Ministry of Education, Culture, Sports, Science and Technology of Japan.

■ REFERENCES

(1) Navrotsky, A. *Chem. Mater.* **1998**, *10*, 2787.
(2) Abrahams, S. *Acta Crystallogr., Sect. A* **1994**, *50*, 658.
(3) Hsu, R.; Maslen, E. N.; Boulay, D. d.; Ishizawa, N. *Acta Crystallogr., Sect. B* **1997**, *53*, 420.
(4) Cava, R. J.; Santoro, A.; Murphy, D. W.; Zahurak, S.; Roth, R. S. *J. Solid State Chem.* **1982**, *42*, 251.
(5) Kumada, N.; Kinomura, N. *Mater. Res. Bull.* **1990**, *25*, 881.
(6) Kumada, N.; Hosoda, S.; Muto, F.; Kinomura, N. *Inorg. Chem.* **1989**, *28*, 3592.
(7) Syono, Y.; Akimoto, S.-I.; Ishikawa, Y.; Endoh, Y. *J. Phys. Chem. Solids* **1969**, *30*, 1665.
(8) Ito, E.; Matsui, Y. *Phys. Chem. Miner.* **1979**, *4*, 265.
(9) Ko, J.; Prewitt, C. *Phys. Chem. Miner.* **1988**, *15*, 355.
(10) Ross, N. L.; Ko, J.; Prewitt, C. T. *Phys. Chem. Miner.* **1989**, *16*, 621.
(11) Syono, Y.; Sawamoto, H.; Akimoto, S. *Solid State Commun.* **1969**, *7*, 713.
(12) Leinenweber, K.; Utsumi, W.; Tsuchida, Y.; Yagi, T.; Kurita, K. *Phys. Chem. Miner.* **1991**, *18*, 244.
(13) Mehta, A.; Leinenweber, K.; Navrotsky, A.; Akaogi, M. *Phys. Chem. Miner.* **1994**, *21*, 207.
(14) Leinenweber, K.; Linton, J.; Navrotsky, A.; Fei, Y.; Parise, J. B. *Phys. Chem. Miner.* **1995**, *22*, 251.
(15) Hattori, T.; Matsuda, T.; Tsuchiya, T.; Nagai, T.; Yamanaka, T. *Phys. Chem. Miner.* **1999**, *26*, 212.
(16) Linton, J. A.; Fei, Y.; Navrotsky, A. *Am. Mineral.* **1997**, *82*, 639.
(17) Leinenweber, K.; Wang, Y.; Yagi, T.; Yusa, H. *Am. Mineral.* **1994**, *79*, 197.
(18) Akaogi, M.; Kojitani, H.; Yusa, H.; Yamamoto, R.; Kido, M.; Koyama, K. *Phys. Chem. Miner.* **2005**, *32*, 603.
(19) Yusa, H.; Akaogi, M.; Sata, N.; Kojitani, H.; Yamamoto, R.; Ohishi, Y. *Phys. Chem. Miner.* **2006**, *33*, 217.
(20) Funamori, N.; Yagi, T.; Miyajima, N.; Fujino, K. *Science* **1997**, *275*, 513.
(21) Sleight, A. W.; Prewitt, C. T. *Mater. Res. Bull.* **1970**, *5*, 207.
(22) Inaguma, Y.; Yoshida, M.; Katsumata, T. *J. Am. Chem. Soc.* **2008**, *130*, 6704.
(23) Aimi, A.; Katsumata, T.; Mori, D.; Fu, D.; Itoh, M.; Kyômen, T.; Hiraki, K.; Takahashi, T.; Inaguma, Y. *Inorg. Chem.* **2011**, *50*, 6392.
(24) Inaguma, Y.; Yoshida, M.; Tsuchiya, T.; Aimi, A.; Tanaka, K.; Katsumata, T.; Mori, D. *J. Phys.: Conf. Ser.* **2010**, *215*, 012131.
(25) Utsumi, W.; Funakoshi, K.; Katayama, Y.; Yamakata, M.; Okada, T.; Shimomura, O. *J. Phys.: Condens. Matter* **2002**, *14*, 10497.
(26) Izumi, F.; Momma, K. *Solid State Phenomena* **2007**, *130*, 15.
(27) Momma, K.; Izumi, F. *J. Appl. Crystallogr.* **2008**, *41*, 653.
(28) Weidner, D. J.; Wang, Y.; Vaughan, M. T. *Science* **1994**, *266*, 419.
(29) Saitoh, H.; Utsumi, W.; Kaneko, H.; Aoki, K. *Jpn. J. Appl. Phys.* **2004**, *43*, L981.
(30) Yagi, T.; Akimoto, S.-i. *J. Geophys. Res.* **1980**, *85*, 6991.
(31) Nishiyama, G.; Hayashi, H. *Nagoya Kogyo Gijutsu Shikensho Hokoku* **1981**, *30*, 75.
(32) Brown, I. D.; Shannon, R. D. *Acta Crystallogr., Sect. A* **1973**, *29*, 266.
(33) Altermatt, D.; Brown, I. D. *Acta Crystallogr., Sect. B* **1985**, *41*, 240.
(34) Brown, I. D.; Altermatt, D. *Acta Crystallogr., Sect. B* **1985**, *41*, 244.
(35) Brese, N. E.; O'Keeffe, M. *Acta Crystallogr., Sect. B* **1991**, *47*, 192.
(36) Nesbitt, H. W.; Legrand, D.; Bancroft, G. M. *Phys. Chem. Miner.* **2000**, *27*, 357.
(37) Kohn, K.; Inoue, K.; Horie, O.; Akimoto, S.-I. *J. Solid State Chem.* **1976**, *18*, 27.
(38) Subramanian, M. A.; Ramirez, A. P.; Marshall, W. J. *Phys. Rev. Lett.* **1999**, *82*, 1558.
(39) Munoz, A.; Alonso, J. A.; Martinez-Lope, M. J.; Falcon, H.; Garcia-Hernandez, M.; Moran, E. *Dalton Trans.* **2006**, 4936.
(40) Alonso, J. A.; Martínez-Lopea, M. J.; Callea, C. d. l.; Muñozb, A.; Moránc, E.; Demazeaud, G. *J. Phys.: Conf. Ser.* **2008**, *121*, 032004.
(41) Ishiwata, S.; Azuma, M.; Takano, M. *Chem. Mater.* **2007**, *19*, 1964.
(42) Shirane, G.; Suzuki, K. *J. Phys. Soc. Jpn.* **1951**, *6*, 274.
(43) Shirane, G.; Pepinsky, R.; Frazer, B. C. *Phys. Rev.* **1955**, *97*, 1179.
(44) Belik, A. A.; Azuma, M.; Saito, T.; Shimakawa, Y.; Takano, M. *Chem. Mater.* **2004**, *17*, 269.
(45) Shpanchenko, R. V.; Chernaya, V. V.; Tsirlin, A. A.; Chizhov, P. S.; Sklovsky, D. E.; Antipov, E. V.; Khlybov, E. P.; Pomjakushin, V.; Balagurov, A. M.; Medvedeva, J. E.; Kaul, E. E.; Geibel, C. *Chem. Mater.* **2004**, *16*, 3267.
(46) Oka, K.; Yamada, I.; Azuma, M.; Takeshita, S.; Satoh, K. H.; Koda, A.; Kadono, R.; Takano, M.; Shimakawa, Y. *Inorg. Chem.* **2008**, *47*, 7355.
(47) DeVries, R. C.; Roth, W. L. *J. Am. Ceram. Soc.* **1968**, *51*, 72.
(48) Chamberland, B. L.; Moeller, C. W. *J. Solid State Chem.* **1972**, *5*, 39.
(49) Arévalo-López, A. M.; Dos santos-García, A. J.; Alario-Franco, M. A. *Inorg. Chem.* **2009**, *48*, 5434.
(50) Arévalo-López, Á. M.; Alario-Franco, M. Á. *J. Solid State Chem.* **2007**, *180*, 3271.

(51) Oka, K.; Azuma, M.; Hirai, S.; Belik, A. A.; Kojitani, H.; Akaogi, M.; Takano, M.; Shimakawa, Y. *Inorg. Chem.* **2009**, *48*, 2285.
(52) Tsuchiya, T.; Saito, H.; Yoshida, M.; Katsumata, T.; Ohba, T.; Inaguma, Y.; Tsurui, T.; Shikano, M. *Mater. Res. Soc. Symp. Proc.* **2007**, *988E*, 0988.
(53) Kafalas, J. A.; Longo, J. M. *Mater. Res. Bull.* **1970**, *5*, 193.
(54) Kimber, S. A. J.; Rodgers, J. A.; Wu, H.; Murray, C. A.; Argyriou, D. N.; Fitch, A. N.; Khomskii, D. I.; Attfield, J. P. *Phys. Rev. Lett.* **2009**, *102*, 046409.
(55) Cheng, J. G.; Zhou, J. S.; Goodenough, J. B. *Phys. Rev. B* **2009**, *80*, 174426.
(56) Burns, R. G. *Mineralogical Applications of Crystal Field Theory*, 2nd ed.; Cambridge University Press: New York, 1993.
(57) Megaw, H. D. *Crystal Structures: A Working Approach*; Saunders: Philadelphia, PA, 1973.
(58) Sasaki, S.; Prewitt, C. T.; Bass, J. D.; Schulze, W. A. *Acta Crystallogr., Sect. C* **1987**, *43*, 1668.
(59) Dann, S. E.; Currie, D. B.; Weller, M. T.; Thomas, M. F.; Al-Rawwas, A. D. *J. Solid State Chem.* **1994**, *109*, 134.
(60) Glazer, A. *Acta Crystallogr., Sect. B* **1972**, *28*, 3384.
(61) Glazer, A. *Acta Crystallogr., Sect. A* **1975**, *31*, 756.
(62) Syono, Y.; Akimoto, S. *Mater. Res. Bull.* **1968**, *3*, 153.
(63) Filatov, S.; Bendeliani, N.; Albert, B.; Kopf, J.; Dyuzeva, T.; Lityagina, L. *Solid State Sci.* **2005**, *7*, 1363.
(64) D'Antonio, P.; Santoro, A. *Acta Crystallogr., Sect. B* **1980**, *36*, 2394.
(65) Rosseinsky, M. J.; Prassides, K. *Acta Crystallogr., Sect. C* **1991**, *47*, 2519.
(66) Yeom, Y. H.; Kim, Y.; Seff, K. *Microporous Mesoporous Mater.* **1999**, *28*, 103.
(67) Sasaki, S.; Fujino, K.; Takeuchi, Y. *Proc. Jpn. Acad., Ser. B* **1979**, *55*, 43.

NOTE ADDED AFTER ASAP PUBLICATION

The unnumbered equation describing distortions of NiO_6 octahedra has been corrected and this paper reposted October 3, 2011.